Stability Criterion for Inertial and Primary Frequency Droop Control in MTDC Grids with Implications on Ratio-based Frequency Support

Sai Gopal Vennelaganti, *Student Member, IEEE*, and Nilanjan Ray Chaudhuri, *Senior Member, IEEE*

***Abstract*—Multiple strategies have been proposed to exchange frequency support amongst asynchronous AC areas through Multiterminal DC (MTDC) grid. Majority of these strategies rely on basic droop control mechanisms involving either inertial or primary frequency droop, or both. This paper addresses the requirements on those droop coefficients, which ensure small-signal stability. To that end, a stability criterion is hypothesized based on certain observations. Using a reduced Nth-order model, the hypothesis is analytically proved for the cases when either inertial droop or primary frequency droop control is active. Moreover, implication of this hypothesis on a recently proposed ratio-based frequency support method is analyzed to derive new stability constraints over and above the existing performance requirements. To support the stability hypothesis, numerically constructed stability boundaries in the droop coefficient space are studied. The stability boundary obtained from small-signal analysis of the full-order nonlinear model is shown to approximately match the boundary obtained from the Nth-order model, which further strengthens the hypothesis. Finally, various time-domain simulation studies are performed on full-order model to validate the stability hypothesis.**

***Index Terms*—MTDC, Stability, Droop, HVDC, Inertial Support, Frequency Support, Stability Boundary**

I. Introduction

IN 2019, two near-simultaneous outages of a generating unit and a wind farm in the UK caused a significant drop in frequency, which activated under-frequency load shedding and eventually caused a blackout that left almost a million homes across the country in the dark and has seriously affected the transportation network. Provision of frequency support from the continental European grid and Ireland through a Multiterminal DC (MTDC) grid has the potential to prevent such blackouts. Therefore, it is important to study the process of exchange of frequency support through MTDC grid. Despite the existence of quite a few techniques and strategies to provide frequency support through MTDC in the literature, traditional droop-based controllers are the most popular in industry due to their simplicity. However, to the best of our knowledge, analytical stability constraints and fundamental understanding of stability aspects of such an interconnected AC-DC system with frequency droop control has not been reported. To bridge that gap, this paper focuses on stability of AC-DC system that are equipped with traditional droop-based inertial and primary frequency controllers.

Various control strategies present in literature can be broadly divided into two types, (i) centralized and distributed modern controllers and (ii) traditional droop-based controllers. References [1]–[7] have proposed strategies that fall into the prior category. Papers [1] and [2] proposed two similar consensus-based controllers and analytically proved system stability with identical asynchronous AC system assumption. Building on these, [3], [4] proposed a distributed proportional-integral controller and a distributed model predictive control (MPC), respectively. References, [5], [6] proposed distributed controllers for secondary frequency support. In these papers [3]–[6], small-signal stability of the closed-loop system was analytically proved. On the other hand, [7] proposed MPC for AGC action, albeit, did not perform any stability analysis. Instead, parameters were designed by trial and error to get a stable and damped response.

The concept of using droop control to provide frequency support through MTDC grid was first proposed in [8]. The idea of providing such support from offshore wind farms (OWFs) is reported in [9]. Inspired by [8], [9], various droop-based control techniques were proposed in literature [10]–[24]. However, in contrast to the previously mentioned modern control techniques, despite the simplicity and widespread use of droop control, none of the works [8]–[24] on droop-based frequency support through MTDC grid have analytically established stability with respect to the choice of inertial or primary frequency droop coefficients. Only reference [6] proved the stability of power-frequency-voltage (DC-side voltage) droop, which is obtained as a special case of the distributed controller that the paper proposed. On the other hand, references [11], [12], [20], [24] have performed rootlocus-based numerical small-signal stability analysis, which is not comparable to analytical proof of stability that holds across multiple operating points. The current state of stability analysis performed in literature on controllers that provide frequency support is summarized in Table I.

Recently, a frequency support method was proposed in [22]–[24], which aims to achieve a prescribed ratio among the frequency deviations of participating areas. This requirement was first introduced in the context of steady-state deviations in [22]. In [23], the criterion was extended by imposing a prescribed ratio among the frequency deviations of the asynchronous areas even during the dynamic conditions. In addition, this paper presented a provision for 'selective' participation of converters in frequency support service. Reference [24] achieved the ratio-

The authors are with the School of Electrical Engineering and Computer Science, Pennsylvania State University, State College, PA, USA (e-mail: *suv66@psu.edu* and *nuc88@engr.psu.edu*).

Financial support from NSF Grant Award ECCS 1656983 is gratefully acknowledged.

TABLE I
STABILITY ANALYSIS ON VARIOUS CONTROLLERS IN LITERATURE THAT PROVIDE FREQUENCY SUPPORT THROUGH MTDC GRIDS

Literature		***Controller Description***	***Stability Analysis***
Modern Centralized and Distributed Controllers	[1], [2]	Consensus-based controllers	Analytically proved for a special case
	[3]	Distributed proportional-integral control	Analytically proved
	[4]	Distributed MPC	Analytically proved
	[5], [6]	Distributed controllers for secondary frequency support	Analytically proved
	[7]	MPC for AGC action	Designed by trial and error
Traditional Droop-based Controllers	[8]	First proposed droop to provide frequency support in MTDC	No stability analysis
	[9]	Droop to extract support from OWFs	No stability analysis
	[8]–[24]	Various droop-based controls	Only [11], [12], [20], [24] have performed numerical rootlocus analysis

based criterion for all time after the disturbance in a reduced Nth-order system and extended the strategy to incorporate OWFs. Such a performance requirement could be vital in view of the future market mechanisms. However, constraints guaranteeing AC-DC system stability in conjunction with the performance requirement have not been derived in these papers. To fill this gap, this paper presents a small-signal stability criterion for inertial and primary frequency droop control in MTDC grids and examines its implications on the ratio-based control proposed in [22]–[24].

The paper is organized as follows. First, the reduced Nth-order model proposed in [23], which captures frequency dynamics of a generic N-asynchronous AC system is reviewed. Next, modes of operation of droop controls, along with certain observations with respect to the choice of droop coefficients are presented. The observations lead to the 'stability hypothesis,' which is later analytically proved for two modes of operation. In Section IV, the recently-proposed ratio-based frequency support method is reviewed and implications of 'stability hypothesis' on it are presented in Section V. To validate the stability hypothesis, numerically constructed stability boundaries in the droop coefficient space are studied and are compared with stability boundary obtained from small-signal analysis of full-order nonlinear model in Section VI. Finally, various time-domain simulation studies are performed on full-order model to support the stability hypothesis.

II. NTH-ORDER MODEL OF A GENERIC N-ASYNCHRONOUS AC AREA SYSTEM

Figure 1(a) represents a generic N-asynchronous AC area system connected through a meshed MTDC grid. Each converter station connected to an AC area is equipped with a power-frequency-inertial-voltage droop controller as shown in Fig. 1(b). This controller ensures that power injected into AC Area #i through the converter station from MTDC grid, P_{Ci} is given by (1), when dynamics of the PI controller in Fig. 1(b) is neglected, i.e., instantaneous tracking is assumed.

$$P_{Ci} = P_{refi} + k_{fi}\Delta f_i - 2h_i f_i \dot{f}_i + k_{vi}(V_{DCcom}^2 - V_{DCref}^2)/4 \quad (1)$$

Here, $\Delta f_i = f_0 - f_i$ denotes the frequency deviation from nominal value f_0, and P_{refi} denotes the total reference power of converters in ith area. The parameters k_{fi}, h_i, and k_{vi}

(a) Generic N-Asynchornous AC Area System:

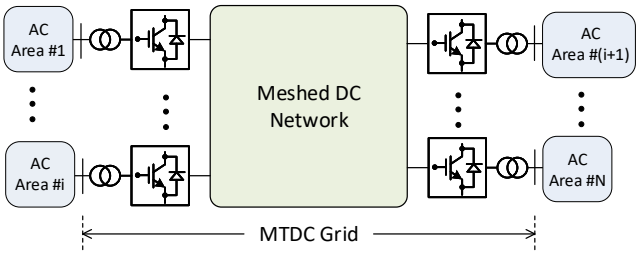

(b) Inertial and Frequency Droop Controller in Area #i:

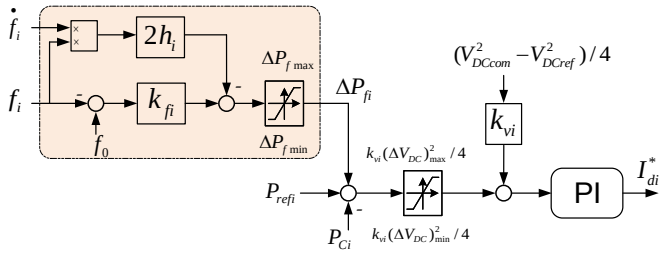

Fig. 1. Representation of (a) a generic N-asynchronous AC area system connected through meshed MTDC network and (b) the power-frequency-inertial-voltage droop controller in ith AC area.

represent the primary frequency, inertial, and DC voltage droop coefficients, respectively. Henceforth, the term 'frequency droop' will imply 'primary frequency droop' in this paper, and vice-versa. In this work, voltage measured from a common node, V_{DCcom} in the DC grid is communicated to all the converters for autonomous power sharing [25] with V_{DCref} as its reference.

The objective of the Nth-order model is to capture the frequency dynamics in N-asynchronous AC area system through a simplified reduced-order model. This model was derived in [24], and is briefly reviewed here for the sake of completeness. In reference [24], the following simplifying assumptions were made,

1) Every AC area in Fig. 1(a) is represented with a load, P_{Li} and a lossless synchronous generator (power input, P_{Mi} and inertial constant, H_{Gi}), which is equipped with a governor (inverse droop coefficient, k_{govi}).
2) Dynamics and losses in the DC lines are neglected and only the power-sharing effect of DC voltage droop control

is considered.

3) Control loop dynamics in the converter stations are neglected and instantaneous tracking is assumed enabling the use of equation (1).

With these assumptions, the equations governing the frequency dynamics of the Nth-order model can be derived as,

$$\begin{aligned} &2[H_{Gi}+(1-\bar{k}_{vi})h_i]f_0\dot{f}_i-\bar{k}_{vi}(\sum_{k\neq i}^{N}2h_kf_0\dot{f}_k)\\ &\quad=[k_{govi}+(1-\bar{k}_{vi})k_{fi}]\Delta f_i-\bar{k}_{vi}(\sum_{k\neq i}^{N}k_{fk}\Delta f_k)+\Delta P_i \end{aligned} \tag{2}$$

where, i varies from 1 to N; $\bar{k}_{vi}=k_{vi}/\sum_k^N k_{vk}$ is the normalized voltage-droop coefficient, and ΔP_i is given by,

$$\Delta P_i=P_{Mi}-P_{Li}+P_{refi}-\bar{k}_{vi}(\sum_{k}^{N}P_{refk}) \tag{3}$$

The set of N equations in (2) can be represented in a matrix-vector form as follows, (note that $\Delta f_i=f_0-f_i$ implies, $\dot{f}_i=-\Delta\dot{f}_i$)

$$2f_0\mathbf{H_N}\Delta\dot{\mathbf{f}}=-\mathbf{K_N}\Delta\mathbf{f}-\mathbf{\Delta P} \tag{4}$$

Here, the i^{th} elements of vectors $\mathbf{\Delta P}$ and $\mathbf{\Delta f}$ are ΔP_i and Δf_i, respectively. The matrices $\mathbf{H_N}$ and $\mathbf{K_N}$ have similar structures and their elements are given by,

$$\begin{aligned} H_N(i,j)&=\begin{cases} H_{Gi}+(1-\bar{k}_{vi})h_i & \text{if } i=j\\ -\bar{k}_{vi}h_j & \text{if } i\neq j\end{cases}\\ K_N(i,j)&=\begin{cases} k_{govi}+(1-\bar{k}_{vi})k_{fi} & \text{if } i=j\\ -\bar{k}_{vi}k_{fj} & \text{if } i\neq j\end{cases} \end{aligned} \tag{5}$$

III. Stability Hypothesis for Nth-order Model

The main objective of this paper is to analytically determine the constraints on inertial and frequency droop coefficients (h_i and k_{fi}), for which the linear system (4) is small-signal stable. In order to achieve that objective, a stability criterion is hypothesized based on certain observations. However, before explaining the observations leading to the hypothesis, various modes of operation of the inertial-frequency droop control are presented in the following section.

A. Modes of Operation and Requirement for Stability:

Three modes of frequency support and respective constraints that each needs to satisfy to ensure small-signal stability are described next.

(i) Mode I: Only primary frequency support: The inertial droop coefficients are set to zero in equation (4). Therefore, frequency dynamics is governed by, $2f_0\,\mathbf{H_N}|_{h_i=0:\forall i}\,\Delta\dot{\mathbf{f}}=-\mathbf{K_N}\Delta\mathbf{f}-\mathbf{\Delta P}$. This is the most common form of droop-based frequency support found in literature. For this system to be small-signal stable, the real part of eigenvalues of system matrix should be negative. Using the fact that for any square matrix $\mathbf{A}$, $\text{eig}(-\mathbf{A})=-\text{eig}(\mathbf{A})$, the stability condition is simplified to obtain constraint (6) as follows,

$$\Re(\text{eig}(\hat{\mathbf{K}}_\mathbf{N}))>\mathbf{0} \tag{6}$$

Here, $\hat{\mathbf{K}}_\mathbf{N}=(\mathbf{H_N}|_{h_i=0:\forall i})^{-1}\mathbf{K_N}$.

(ii) Mode II: Only inertial support: Similar to Mode I, frequency droop coefficients are set to zero in equation (4). Therefore, the frequency dynamics is governed by, $2f_0\mathbf{H_N}\Delta\dot{\mathbf{f}}=-\mathbf{K_N}|_{k_{fi}=0:\forall i}\,\Delta\mathbf{f}-\mathbf{\Delta P}$. For this system to be stable, constraint (7) has to be satisfied.

$$\Re(\text{eig}(\hat{\mathbf{H}}_\mathbf{N}))>\mathbf{0} \tag{7}$$

Similar to Mode I, here, $\hat{\mathbf{H}}_\mathbf{N}=(\mathbf{K_N}|_{k_{fi}=0:\forall i})^{-1}\mathbf{H_N}$.

(iii) Mode III: Both Inertial and primary frequency support: During this mode the frequency dynamics is governed by (4). Therefore, for this system to be stable, constraint (8) has to be satisfied.

$$\Re(\text{eig}((\mathbf{H_N})^{-1}\mathbf{K_N}))>\mathbf{0} \tag{8}$$

Clearly, the choice of droop coefficients affects the stability in all three modes. The aim is to determine the inertial and frequency droop coefficients that satisfy either one of the three constraints (6) – (8) depending on the mode of operation. Note that Mode I and Mode II are two special cases of a more general case, Mode III. Therefore, the frequency and inertial droop coefficients, which satisfy (6) and (7), do not necessarily satisfy (8). Nevertheless, the stability hypothesis is formulated for all three modes by observing droop coefficients that satisfy (6) and (7). Moreover, the formal analytical proof of the stability hypothesis is performed only for Modes I and II. However, nonlinear time-domain simulations build the confidence in the accuracy of the same stability hypothesis for Mode III.

B. Observations Leading to Stability Hypothesis:

As mentioned above, all the observations leading to the formulation of the stability hypothesis are made from constraints (6) and (7). In fact, the matrices in these constraints can be represented by a generic matrix, $\hat{\mathbf{X}}_\mathbf{N}$, which makes the analysis easier. The structure of $\hat{\mathbf{X}}_\mathbf{N}$ and definitions of the generic variables in the matrix are presented in equation (9). Next, eigenvalues of this matrix are determined for some specific values of x_i.

1) Observation-I: Substituting $x_i=-C_i\ \forall\ i$, we get,

$$\hat{\mathbf{X}}_\mathbf{N}|_{(x_i=-C_i)}=\hat{\mathbf{k}}_\mathbf{D}\begin{bmatrix}C_1 & \cdots & C_N\end{bmatrix} \tag{10}$$

where, $\hat{\mathbf{k}}_\mathbf{D}=[\bar{k}_{v1}/D_1,\cdots,\bar{k}_{vN}/D_N]^T$. This implies that the above matrix has $N-1$ zero eigenvalues and one positive real eigenvalue, which is given by $\sum_{k=1}^N\bar{k}_{vk}C_k/D_k$. Therefore, for this set of droop coefficients, the system is marginally stable.

2) Observation-II: Substituting $x_i=-C_i+pD_i\ \forall\ i$, where $p>0$ is some positive real constant, we get,

$$\hat{\mathbf{X}}_\mathbf{N}|_{(x_i=-C_i+pD_i)}=p\boldsymbol{I_N}+\hat{\mathbf{k}}_\mathbf{D}\begin{bmatrix}C_1-pD_1 & \cdots & C_N-pD_N\end{bmatrix} \tag{11}$$

where, $\boldsymbol{I_N}$ stands for identity matrix of size N. There are $N-1$ positive-real eigenvalues – each of value p and the remaining eigenvalue λ_1 is given by,

$$\begin{aligned}\lambda_1&=p+\sum_{k=1}^{N}\bar{k}_{vk}(C_k-pD_k)/D_k\\&=p-p(\sum_{k=1}^{N}\bar{k}_{vk})+\sum_{k=1}^{N}\bar{k}_{vk}C_k/D_k\end{aligned} \tag{12}$$

$$\hat{\mathbf{X}}_\mathbf{N} = \begin{bmatrix} [C_1 + (1-\bar{k}_{v1})x_1]/D_1 & -\bar{k}_{v1}x_2/D_1 & \cdots & -\bar{k}_{v1}x_N/D_1 \\ -\bar{k}_{v2}x_1/D_2 & [C_2 + (1-\bar{k}_{v2})x_2]/D_2 & \cdots & -\bar{k}_{v2}x_N/D_2 \\ \vdots & \vdots & \ddots & \vdots \\ -\bar{k}_{vN}x_1/D_N & -\bar{k}_{vN}x_2/D_N & \cdots & [C_N + (1-\bar{k}_{vN})x_N]/D_N \end{bmatrix} = \begin{cases} \hat{\mathbf{H}}_\mathbf{N} & \text{if, } (x_i, C_i, D_i) \\ & = (h_i, H_{Gi}, k_{govi}) \\ \hat{\mathbf{K}}_\mathbf{N} & \text{if, } (x_i, C_i, D_i) \\ & = (k_{fi}, k_{govi}, H_{Gi}) \end{cases} \tag{9}$$

Since, $\bar{k}_{vk}$ is the normalized voltage-droop coefficient, we have, $\sum_{k=1}^{N} \bar{k}_{vk} = 1$. This implies, $\lambda_1 = \sum_{k=1}^{N} \bar{k}_{vk} C_k/D_k$, which is the same as the one positive eigenvalue from Observation-I. Therefore, for this set of droop coefficients, the system is stable.

3) Observation-III: Substituting $x_1 = x_{10} > -C_i$ and $x_i = -C_i \ \forall \ i \neq 1$, we get,

$$\begin{aligned} \hat{\mathbf{X}}_\mathbf{N}|_{(x_i=-C_i, \forall i \neq 1; x_1 = x_{10})} = ((C_1 + x_{10})/D_1)\hat{\mathbf{e}}_\mathbf{1}\hat{\mathbf{e}}_\mathbf{1}^\mathbf{T} \\ + \hat{\mathbf{k}}_\mathbf{D} \begin{bmatrix} -x_{10} & C_2 & \cdots & C_N \end{bmatrix} \end{aligned} \tag{13}$$

here, $\hat{\mathbf{e}}_\mathbf{i}$ is a used as a standard notion to represent unit vector along the ith direction. In order to determine the eigenvalues of the above matrix, we can arrive at the following characteristic polynomial through some algebraic manipulations,

$$\begin{aligned} \lambda^{N-2}\Big[\lambda^2 - \Big(\frac{C_1 + (1-\bar{k}_{v1})x_{10}}{D_1} + \sum_{k=2}^{Nr} \bar{k}_{vk}\frac{C_k}{D_k}\Big)\lambda \\ + \Big(\frac{C_1 + x_{10}}{D_1}\Big)\Big(\sum_{k=2}^{N} \bar{k}_{vk}\frac{C_k}{D_k}\Big)\Big] = 0 \end{aligned} \tag{14}$$

There are $N-2$ zero eigenvalues and the remaining two non-zero eigenvalues say, λ_1 and λ_2, can be obtained by solving the quadratic polynomial part in the above equation. Nonetheless, it is sufficient to know the sum and the product of these two non-zero eigenvalues, which are given by,

$$\begin{aligned} \lambda_1 + \lambda_2 &= \frac{C_1 + (1-\bar{k}_{v1})x_{10}}{D_1} + \sum_{k=2}^{Nr} \bar{k}_{vk}\frac{C_k}{D_k} \\ \lambda_1\lambda_2 &= \Big(\frac{C_1 + x_{10}}{D_1}\Big)\Big(\sum_{k=2}^{N} \bar{k}_{vk}\frac{C_k}{D_k}\Big) \end{aligned} \tag{15}$$

Observe that both the sum and product of the eigenvalues are positive, i.e., $\lambda_1 + \lambda_2 > 0$ and $\lambda_1\lambda_2 > 0$ (recall that $\bar{k}_{v1} < 1$ and $x_{10} > -C_i$). This implies that both the eigenvalues are positive when real or have a positive real part when they are a complex conjugate pair. Either way, the system will be marginally stable with these droop coefficients.

4) Observation-IV: Substituting $x_1 = x_{10} + pD_1$ and $x_i = -C_i + pD_i \ \forall \ i \neq 1$, where $x_{10} > -C_1$ and $p > 0$ is some positive real constant, we get,

$$\begin{aligned} \hat{\mathbf{X}}_\mathbf{N}|_{(x_i=-C_i+pD_i, \forall i \neq 1; x_1 = x_{10}+pD_1)} = ((C_1 + x_{10})/D_1)\hat{\mathbf{e}}_\mathbf{1}\hat{\mathbf{e}}_\mathbf{1}^\mathbf{T} \\ + p\boldsymbol{I}_\boldsymbol{N} + \hat{\mathbf{k}}_\mathbf{D} \begin{bmatrix} -x_{10} - pD_1 & C_2 - pD_2 & \cdots & C_N - pD_N \end{bmatrix} \end{aligned} \tag{16}$$

Using the similar arguments as that of Observation-III, it can be concluded that there are $N-2$ positive-real eigenvalues, each of whose value is p, and two eigenvalues λ_1 and λ_2 satisfying,

$$\begin{aligned} \lambda_1 + \lambda_2 &= \frac{C_1 + (1-\bar{k}_{v1})x_{10}}{D_1} + \sum_{k=2}^{N} \bar{k}_{vk}\frac{C_k}{D_k} + p \\ \lambda_1\lambda_2 &= \Big(\frac{C_1 + x_{10}}{D_1}\Big)\Big(\sum_{k=2}^{N} \bar{k}_{vk}\frac{C_k}{D_k}\Big) + p\Big(\sum_{k=1}^{N} \bar{k}_{vk}\frac{C_k}{D_k}\Big) \end{aligned} \tag{17}$$

Similar to Observation-III, we have sum and product of λ_1 and λ_2 to be positive. This implies that real parts of these eigenvalues are positive. Therefore, this choice of droop coefficients renders the system stable. Going forward, the results from these observations will be summarized, which enables us to hypothesize a stability criterion for the droop coefficients.

C. Statement of Stability Hypothesis:

If we construct a coordinate system in the droop coefficient space with origin at $x_i = -C_i \ \forall \ i$ and assign the unit vectors $\hat{e}_i$s as the basis vectors, then the choice of droop coefficient in observations made above indicate the following,

1) The origin $x_i = -C_i \ \forall \ i$ and points along any positive axis result in a marginally stable system.
2) Starting from any of the above-stated marginally stable points, moving in the direction of vector $[D_1, \cdots, D_N]^T$ into the positive quadrant of the constructed coordinate system makes the system stable.

Building on the above-made observations, the 'stability hypothesis' is presented next.

Stability Hypothesis: Choosing the inertial and frequency droop coefficients such that, $h_i = -H_{Gi} + u_i$ and $k_{fi} = -k_{govi} + v_i$ (i.e., $x_i = -C_i + p_i$), where $u_i > 0$ and $v_i > 0$ (i.e., $p_i > 0$) $\forall \ i$, ensures the system is small-signal stable, i.e., constraints (6) – (8) will be satisfied.

In other words, starting from the marginally stable points, i.e., origin $x_i = -C_i \ \forall \ i$ or the points on any positive axis and moving into the positive quadrant of the constructed coordinate system (not just along the vector $[D_1, \cdots, D_N]^T$) makes the system asymptotically stable.

D. Formal Proof of the Hypothesis for Mode I and Mode II:

Based on a lemma, which is supported by continuity arguments, a formal proof of the proposed hypothesis is presented for Mode I and Mode II. Next, the lemma is stated and proved.

Lemma-I: Given a matrix, $\mathbf{M}(\boldsymbol{\tau})$ such that, all its elements are continuous functions of parameter $\boldsymbol{\tau} \in \mathbb{R}^n$ $\big($i.e, $\mathbf{M}(\boldsymbol{\tau}) = [m_{ij}(\boldsymbol{\tau})]$, where m_{ij} is continuous w.r.t. $\boldsymbol{\tau} \ \forall \ i, j\big)$, then $\Re(\text{eig}(\mathbf{M}(\boldsymbol{\tau}))) < \mathbf{0} \ \forall \ \boldsymbol{\tau} \in \mathcal{S} \subseteq \mathbb{R}^n$, if the region $\mathcal{S}$ satisfies the following conditions,

1) $\mathcal{S}$ is connected,

2) $\exists$ at least one $\boldsymbol{\tau^*} \in \mathcal{S}$ s.t. $\Re(\text{eig}(\mathbf{M}(\boldsymbol{\tau^*}))) < \mathbf{0}$, and
3) $\nexists\ \boldsymbol{\tau} \in \mathcal{S}$, s.t. at least one eigenvalue of $\mathbf{M}(\boldsymbol{\tau})$ has zero real part.

Remark-I: Before presenting the proof of this lemma, an important consequence of matrix elements being continuous functions of parameter $\boldsymbol{\tau} \in \mathbb{R}^n$ should be understood. In [26] it is established that zeros of a polynomial are continuous w.r.t. to its coefficients, which implies that eigenvalues of a matrix are continuous w.r.t. its elements. Consequently, the eigenvalues, specifically the real part of the eigenvalues of the matrix $\mathbf{M}(\boldsymbol{\tau})$ are continuous w.r.t. $\boldsymbol{\tau}$.

Proof: For the sake of contradiction, assume that $\exists\ \bar{\boldsymbol{\tau}} \in \mathcal{S}$ s.t. at least one eigenvalue of $\mathbf{M}(\bar{\boldsymbol{\tau}})$ has a positive real part. From condition (2), $\exists\ \boldsymbol{\tau^*} \in \mathcal{S}$ s.t. $\Re(\text{eig}(\mathbf{M}(\boldsymbol{\tau^*}))) < \mathbf{0}$. Since $\boldsymbol{\tau^*}, \bar{\boldsymbol{\tau}} \in \mathcal{S}$, which is a connected region in $\mathbb{R}^n$, we can construct a path, $\mathcal{P}$ between $\boldsymbol{\tau^*}$ and $\bar{\boldsymbol{\tau}}$ s.t. $\mathcal{P} \subseteq \mathcal{S}$. The real part of the eigenvalues should continuously change as we vary $\boldsymbol{\tau}$ along the path, $\mathcal{P}$ from $\boldsymbol{\tau^*}$ to $\bar{\boldsymbol{\tau}}$. This implies that $\exists\ \boldsymbol{\tau^0} \in \mathcal{P} \subseteq \mathcal{S}$ s.t. at least one eigenvalue of $\mathbf{M}(\boldsymbol{\tau^0})$ has zero real part. However, this contradicts condition (3). Hence, by contradiction we have $\Re(\text{eig}(\mathbf{M}(\boldsymbol{\tau}))) < \mathbf{0}\ \forall\ \boldsymbol{\tau} \in \mathcal{S}$.

Theorem-I: Given the matrix $\hat{\mathbf{X}}_\mathbf{N}$, which has the structure shown in (9) with $C_i, D_i, \bar{k}_{vi} > 0\ \forall\ i$ and $\sum_{k=1}^{N} \bar{k}_{vk} = 0$; then the matrix satisfies, $\Re(\text{eig}(\hat{\mathbf{X}}_\mathbf{N})) > \mathbf{0}$, if $x_i > -C_i\ \forall\ i$.

Proof: Let $\mathbf{x} \in \mathbb{R}^N$ s.t. its ith entry is x_i. The elements of matrix $-\hat{\mathbf{X}}_\mathbf{N}$ are continuous function of $\mathbf{x}$. In fact they are linear in $\mathbf{x}$. Let us define region $\mathcal{S}_x \triangleq \{\mathbf{x} \mid x_i > -C_i\ \forall\ i\}$. In order to prove that $\Re(\text{eig}(\hat{\mathbf{X}}_\mathbf{N})) > \mathbf{0} \iff \Re(\text{eig}(-\hat{\mathbf{X}}_\mathbf{N})) < \mathbf{0}\ \forall\ \mathbf{x} \in \mathcal{S}_x \subseteq \mathbb{R}^N$, Lemma-I can be used if region $\mathcal{S}_x$ satisfies the three conditions. Clearly, by definition, region $\mathcal{S}_x$ is connected. From Observation-II and Observation-IV, we have multiple $\mathbf{x}^* \in \mathcal{S}_x$, s.t. $\Re(\text{eig}(\hat{\mathbf{X}}_\mathbf{N}(\mathbf{x}^*))) > \mathbf{0}$. For condition (3), if we assume that $\exists\ \mathbf{v} \in \mathbb{R}^N$, s.t. $\hat{\mathbf{X}}_\mathbf{N}\mathbf{v} = \sqrt{-1}\lambda_{im}\mathbf{v}$ for some $\lambda_{im} \in \mathbb{R}$ and $\forall\ \mathbf{x} \in \mathcal{S}_x$, then it can be shown that $\mathbf{v}$ has to be $\mathbf{0}$. Therefore, $\forall\ \mathbf{x} \in \mathcal{S}_x$, we have $\Re(\text{eig}(\hat{\mathbf{X}}_\mathbf{N})) > \mathbf{0}$.

Thus, from Theorem-I we formally proved the stability hypothesis for modes I and II. Numerical validation of the hypothesis for Mode III is presented in Section VII. Next, the focus is shifted onto reviewing the ratio-based frequency support and discussing the implications of this hypothesis on it. Note that we continue calling this a 'stability hypothesis' instead of a 'stability theorem,' since the formal proof for Mode III could not be established in this paper.

IV. Review of Ratio-based Frequency Support

This section summarizes the concept of ratio-based frequency support introduced in references [23] and [24].

A. Objective:

The objective of the ratio-based frequency support is to achieve a prescribed ratio among frequency deviations of the participating areas at all time after the disturbance, while there is no frequency deviation in non-participating areas. In general, this ratio can be prescribed by system operators based on economics and operational constraints. Let N_r be the number of participating areas and let the prescribed ratio be $r_1 : r_2 : \cdots : r_{Nr}$. Without loss of generality, the indexing of areas is done such that the area with AC disturbance is indexed as Area#1 ($\Delta P_1 \neq 0$) and that the non-participating areas are concatenated to the end. Therefore, the desired post-disturbance frequency deviations at any time after disturbance can be represented as,

$$\boldsymbol{\Delta f} = \Big[\underbrace{r_1\Delta f^* \quad r_2\Delta f^* \quad \cdots \quad r_{N_r}\Delta f^*}_{1\times N_r} \underbrace{0 \quad \cdots \quad 0}_{1\times(N-N_r)}\Big]^T \tag{18}$$

Here, the variable f^* is the 'base frequency' and Δf^* is the deviation in base frequency from its nominal value f_0, given by $\Delta f^* = f_0 - f^*$.

B. Proposed Solution:

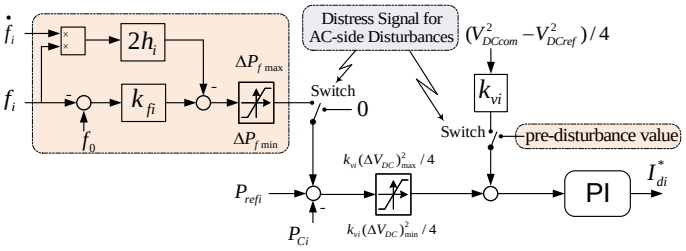

Fig. 2. Representation of aggregated power-frequency-inertial-voltage droop controller in the i^{th} AC area. Inertial-frequency droop (in light pink) is activated when an AC area requests frequency support through distress signal.

The solution [24] to meet the above stated objective is summarized here. In pre-disturbance period, only common-mode DC voltage droop is kept active. Following an AC disturbance, a distress signal is sent from the affected area, see Fig. 2. The converter of other areas receive the distress signal and, based on the area that is seeking help, the non-participating areas would hold their power-levels to the pre-disturbance values. The participating areas on the other hand, will activate the frequency control with inertial and frequency-droop coefficients that satisfy certain performance constraints. In [24], these constraints were derived to ensure that the above-stated ratio-based objective is achieved in the Nth-order model. However, for the sake of completeness, a short proof is added in Appendix B. The constraints are as follows:

$$\mathbf{K_{Nr}}\begin{bmatrix} r_1 & \cdots & r_{N_r}\end{bmatrix}^T = (\sum_{k}^{N_r} r_k k_{govk})\hat{\mathbf{e}}_\mathbf{1} \tag{19}$$

$$\mathbf{H_{Nr}}\begin{bmatrix} r_1 & \cdots & r_{N_r}\end{bmatrix}^T = (\sum_{k}^{N_r} r_k H_{Gk})\hat{\mathbf{e}}_\mathbf{1} \tag{20}$$

The matrices $\mathbf{H_{Nr}}$ and $\mathbf{K_{Nr}}$ are same as $\mathbf{H_N}$ and $\mathbf{K_N}$ described in (5), except for N, which is replaced by N_r and $\bar{k}_{vi}$ is adjusted based on participating areas. The vector $\hat{\mathbf{e}}_\mathbf{1}$, stands for unit vector along the 1st dimension. Constraint (19) independently ensures that the post-disturbance steady-state frequency deviations are in the prescribed ratio (Mode-I : Primary frequency support). Similarly, constraint (20) involving inertial-droop coefficients independently ensures that the prescribed ratio is maintained among the initial slopes of the frequencies (Mode-II : Inertial frequency support). However, to satisfy the prescribed ratio-based criterion for the *entire* duration of the post-disturbance period, both constraints (19) and (20) have to be met (Mode-III : Both primary and inertial frequency support). It is shown in [24] that since these

$$\mathbf{X_{Nr}} = \begin{bmatrix} C_1 + (1-\bar{k}_{v1})x_1 & -\bar{k}_{v1}x_2 & \cdots & -\bar{k}_{v1}x_{Nr} \\ -\bar{k}_{v2}x_1 & C_2 + (1-\bar{k}_{v2})x_2 & \cdots & -\bar{k}_{v2}x_{Nr} \\ \vdots & \vdots & \ddots & \vdots \\ -\bar{k}_{vNr}x_1 & -\bar{k}_{vNr}x_2 & \cdots & C_{Nr} + (1-\bar{k}_{vNr})x_{Nr} \end{bmatrix} = \begin{cases} \mathbf{H_{Nr}} & \text{if, } (x_i, C_i) \\ & = (h_i, H_{Gi}) \\ \hline \mathbf{K_{Nr}} & \text{if, } (x_i, C_i) \\ & = (k_{fi}, k_{govi}) \end{cases} \tag{21}$$

constraints are derived using an Nth-order model, the resulting droop coefficients approximately deliver the desired response in full-order model.

The constraints (19) and (20) can be considered as performance criteria of the system. However, they are derived under the assumption that the closed-loop Nth-order system is stable. In the next section, these performance constraints are combined with the stability constraints obtained from the stability hypothesis.

V. Implications of Stability Hypothesis on Ratio-based Frequency Support

In this section, first a generalized solution to the performance constraints (19) and (20) is derived. On the derived generalized solution, stability requirement from the hypothesis is imposed to determine the droop coefficients that ensure both performance as well as stability.

A. General Solution to the Ratio-based Frequency Performance Constraints:

As shown in (5), matrices $\mathbf{H_{Nr}}$ and $\mathbf{K_{Nr}}$ have the same structure. Therefore, similar to $\hat{\mathbf{X}}_\mathbf{N}$ they can be represented by a generic matrix $\mathbf{X_{Nr}}$, which is presented in (21). Therefore, performance constraints (19) and (20) can be rearranged and expressed by a generic constraint (22). There are multiple solutions to constraint (22) since it has N_r unknowns (x_1, x_2, $\cdots$, x_{Nr}) and $(N_r - 1)$ independent equations. Now, we shall determine the generic form for this solution set.

$$\begin{bmatrix} r_1\bar{k}_{v2} & -r_2(1-\bar{k}_{v2}) & \cdots & r_{N_r}\bar{k}_{v2} \\ r_1\bar{k}_{v3} & r_2\bar{k}_{v3} & \cdots & r_{N_r}\bar{k}_{v3} \\ \vdots & \vdots & \ddots & \vdots \\ r_1\bar{k}_{vNr} & r_2\bar{k}_{vNr} & \cdots & -r_{N_r}(1-\bar{k}_{vNr}) \end{bmatrix} \begin{bmatrix} x_1 \\ x_2 \\ \vdots \\ x_{Nr} \end{bmatrix} = \begin{bmatrix} r_2C_2 & r_3C_3 & \cdots & r_{Nr}C_{Nr} \end{bmatrix}^T \tag{22}$$

Let us define a vector $\vec{x} \in \mathbb{R}^{Nr}$, whose ith component is x_i. The solution set of the jth equation in constraint (22) represents a hyperplane $\mathcal{H}_j \subset \mathbb{R}^{Nr}$, where $j = 2, \cdots, N_r$. The intersection of these sets, $\mathcal{L} = \bigcap_{j=2}^{Nr} \mathcal{H}_j$ denotes the solution set satisfying constraint (22). This set $\mathcal{L}$ represents a line in N_r-dimensional space, which lives on all those $(N_r - 1)$ hyperplanes. From geometry, we know that the parametric equation of this line can be expressed as,

$$\mathcal{L} \triangleq \{\vec{x} = \vec{x}_0 + t\vec{a}_1 \mid t \in \mathbb{R}\} \tag{23}$$

where, $\vec{x}_0$ is any point that is on the line and $\vec{a}_1$ is any vector parallel to this line. Thus, finding any point $\vec{x}_0$ that satisfies constraint (22) and any vector $\vec{a}_1$ that is parallel to the line gives us the parametric representation of the set of solutions to the constraint (22).

From linear algebra we know that the vector $\vec{a}_1$ is perpendicular to all the normals to the respective hyperplanes. This means vector $\vec{a}_1$ should satisfy,

$$\begin{bmatrix} r_1\bar{k}_{v2} & -r_2(1-\bar{k}_{v2}) & \cdots & r_{N_r}\bar{k}_{v2} \\ r_1\bar{k}_{v3} & r_2\bar{k}_{v3} & \cdots & r_{N_r}\bar{k}_{v3} \\ \vdots & \vdots & \ddots & \vdots \\ r_1\bar{k}_{vNr} & r_2\bar{k}_{vNr} & \cdots & -r_{N_r}(1-\bar{k}_{vNr}) \end{bmatrix} \vec{a}_1 = 0 \tag{24}$$

It can be shown that the following vector,

$$\vec{a}_1 = \begin{bmatrix} \bar{k}_{v1}/r_1 & \bar{k}_{v2}/r_2 & \cdots & \bar{k}_{vNr}/r_{Nr} \end{bmatrix}^T \tag{25}$$

satisfies (24). Notice that the vector direction depends both on the desired ratio and DC voltage-droop coefficients, but not on AC-side parameters like, k_{govi} or H_{Gi}.

B. Unification of Generalized Performance Solution and Stability Hypothesis:

From Observation-III, we know that the point of the form, $x_1 = x_{10} > -C_i$ and $x_i = -C_i \; \forall \; i \neq 1$ is marginally stable. Substituting these x_i values in equation (22) reveals that this point qualifies as $\vec{x}_0$, if and only if $x_{10} = \sum_{k=2}^{N_r} r_k C_k / r_1$. Thus, $\vec{x}_0$ shown below results in a marginally stable system,

$$\vec{x}_0 = \begin{bmatrix} \sum_{k=2}^{N_r} r_k C_k / r_1 & -C_2 & \cdots & -C_{Nr} \end{bmatrix}^T \tag{26}$$

Theorem-II: (Unification Theorem) Given $\vec{a}_1$ and $\vec{x}_0$ of the form (25) and (26), respectively, with $r_i > 0$, the subset $\mathcal{L}_s$ to the solution set $\mathcal{L}$ defined as

$$\mathcal{L}_s \triangleq \{\vec{x} = \vec{x}_0 + t\vec{a}_1 \mid t \in \mathbb{R} \text{ and } t > 0\} \subset \mathcal{L} \tag{27}$$

ensures both performance and stability in the Nth-order system.

Proof: This result is quite straightforward and builds upon the prior knowledge. First, since $\mathcal{L}_s$ is a subset of $\mathcal{L}$, which satisfies (22), performance is guaranteed in Nth-order system. Next, since the components of $\vec{a}_1$ are all positive, any ith component of the points in $\mathcal{L}_s$ can be written as, $x_i = -C_i + p_i$ with $p_i > 0$. Therefore, from the stability hypothesis, all points in $\mathcal{L}_s$ guarantee stability of the Nth-order model.

VI. Validation through Numerical Construction of Stability Boundaries for Study System

To further strengthen the stability hypothesis, we will now numerically build surfaces that represent the stability boundary. For this study, test system presented in Fig. 3 is considered. Area#3 in Fig. 3 is operated as a non-participating area throughout this study, i.e., as explained in Section IV it does not contribute to frequency support by holding its power to the pre-disturbance value. In this configuration, the effective inverse governor droops of the participating areas are, $(k_{gov1}, k_{gov2}, k_{gov4}) = (212.20, 53.05, 53.05)$ MW/Hz.

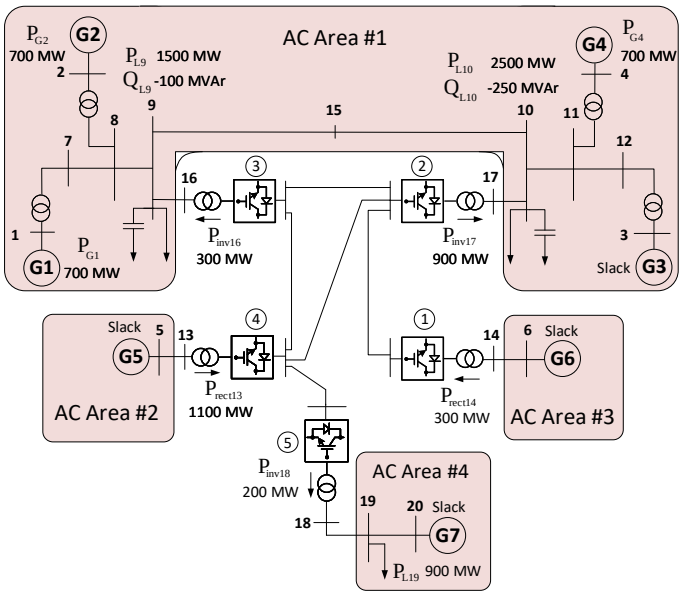

Fig. 3. Study System: Schematic of the bipolar MTDC grid with metallic return (single-line diagram) connecting four asynchronous AC areas.

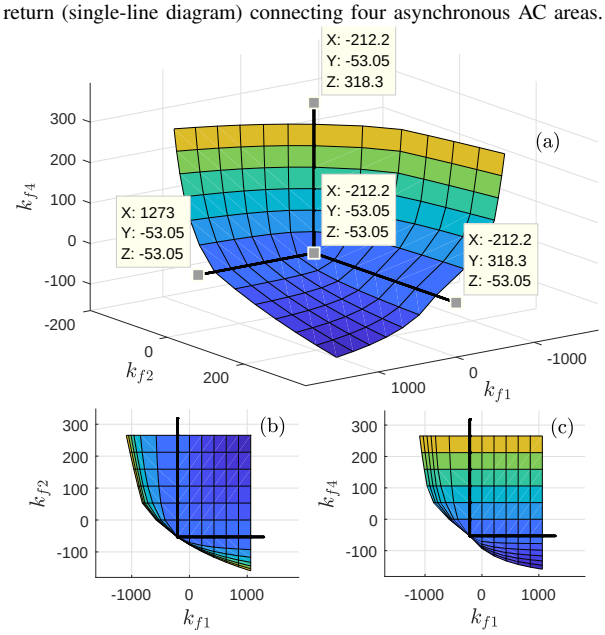

Fig. 4. Stability boundary constructed using the Nth-order model in the k_{fi} space with $h_i = 0\ \forall\ i$: (a) The boundary as viewed from stable region, (b) top view (X-Y view) and (c) side view (X-Z view).

Similarly, the effective inertia constants are (H_{G1}, H_{G2}, H_{G4}) = $(228.15, 185.25, 74.10)\ s^{-1}$ (defined on system, 100 MVA base). Henceforth, frequency and inertial droop coefficients in plots will use MW/Hz and s^{-1} as units.

First, the stability boundary is constructed using the Nth-order model of the test system in Fig. 3 for Modes I and III. The unification theorem (Theorem-II) is then tested by overlapping several performance lines (of the form (23)) on the stability boundary plot, where each of the lines correspond to a particular prescribed ratio. Next, the stability boundary of the Nth-order model is compared with that of the full-order model, which is a realistic representation of the system.

A. Stability Boundary Obtained from Nth-order Model:

Figure 4(a) illustrates the view of stability boundary obtained from the Nth-order model as seen from the stable region.

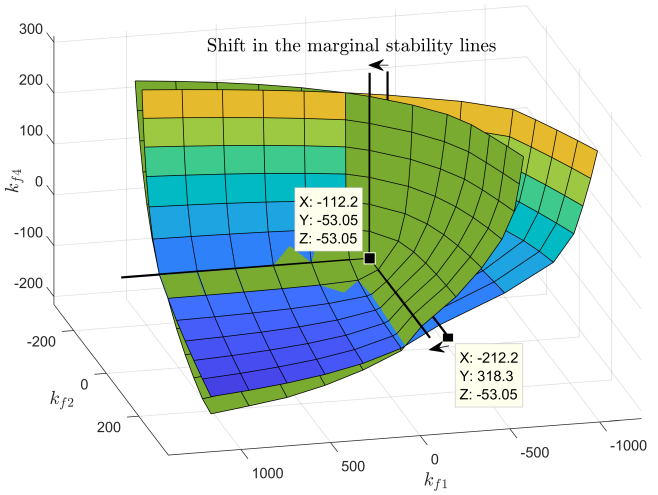

Fig. 5. Shifted stability boundary of Nth-order model due to loss of generation (green) compared against stability boundary of the nominal Nth-order model of the test system (colormap) with $h_i = 0\ \forall\ i$.

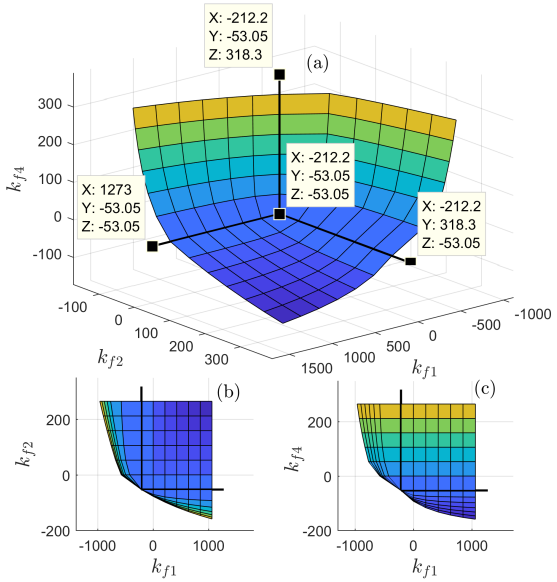

Fig. 6. Stability boundary constructed using the Nth-order model in the k_{fi} space with $h_i > -H_{Gi}$, $h_i \neq 0\ \forall\ i$: (a) The boundary as viewed from stable region, (b) top view (X-Y view) and (c) side view (X-Z view).

Figures 4(b) and (c) present the top and side view of the same, respectively. The X, Y, and Z axes represent various values assumed by k_{f1}, k_{f2}, and k_{f4}, respectively. The entire stability boundary has a concave 3-petal flower like structure, wherein the stable region is on the concave side. The three petals emerge from three rays highlighted by solid lines in Fig. 4. These rays originate from the point $(-k_{gov1}, -k_{gov2}, -k_{gov4})$ and are arranged such that each of them is parallel to X or Y or Z axis. From Observations I and III, we know that all points on the highlighted three rays are marginally stable. Therefore, consistently, these rays belong to the numerically generated stability boundary.

Figure 5 shows the impact of loss of generation in Area#1 ($\Delta k_{gov1} = 100$ and $\Delta H_{G1} = 70$) on the stability boundary of Nth-order model. Since, the stability constraint is $k_{fi} > -k_{govi}$, the marginal stability axis is shifted by Δk_{gov1} as highlighted in Fig. 5. Despite the changes in other regions, the region of interest, i.e., quadrant formed by the three rays is stable.

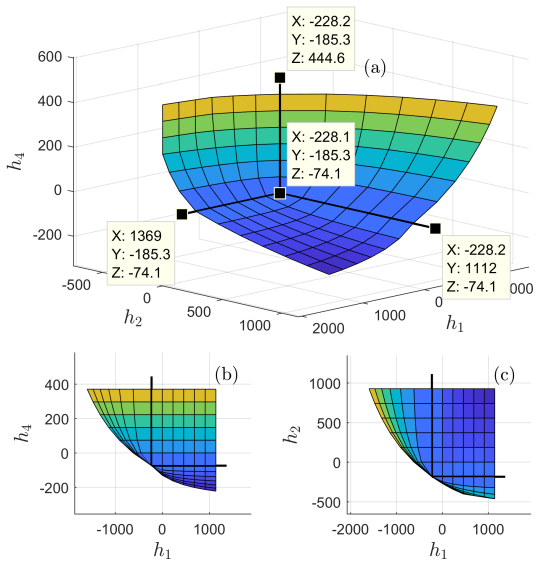

Fig. 7. Stability boundary constructed using the Nth-order model in the h_i space with $k_{fi} > -k_{govi}$, $k_{fi} \neq 0 \ \forall \ i$: (a) The boundary as viewed from stable region, (b) top view (X-Y view) and (c) side view (X-Z view).

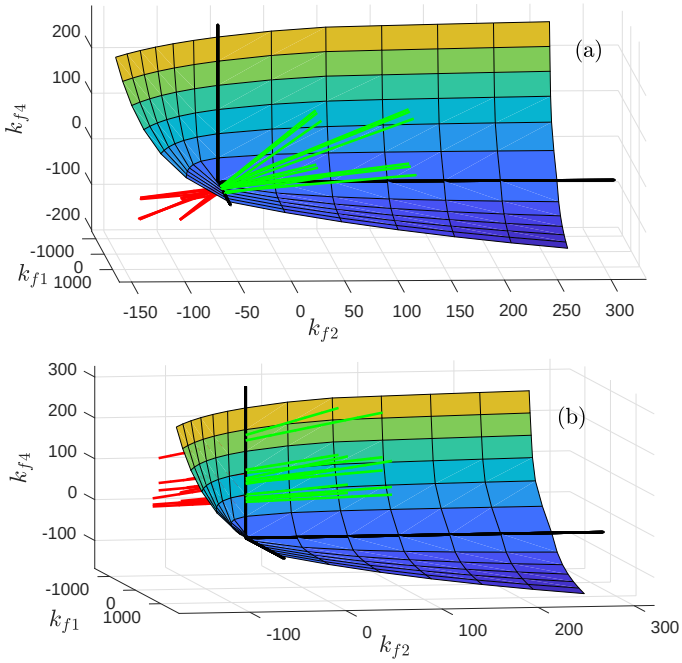

Fig. 8. Performance lines overlapped over the Nth-order model's stability boundary. The lines are plotted for AC disturbances occurring in (a) Area#1 and (b) Area#4, where each line corresponds to a particular prescribed ratio.

The stability boundary for Mode III with 3 participating areas lives in a 6 dimensional space, which is hard to visualize. In order to numerically validate the stability hypothesis for Mode III, two 3D stability boundaries, one in k_{fi} space, and the other in h_i space are presented. Figure 6 illustrates the stability boundary in the k_{fi} space for a random choice of inertia droop coefficients $(h_1, h_2, h_4) = (-178.15, -55.25, -14.10)$ (s.t., $h_i > -H_{Gi} \ \forall \ i \neq 3$). Similarly, Fig. 7 illustrates the stability boundary in the h_i space for a random choice of inertia droop coefficients $(k_{f1}, k_{f2}, k_{f4}) = (-92.21, 36.95, 26.95)$ (s.t., $k_{fi} > -k_{govi} \ \forall \ i \neq 3$).

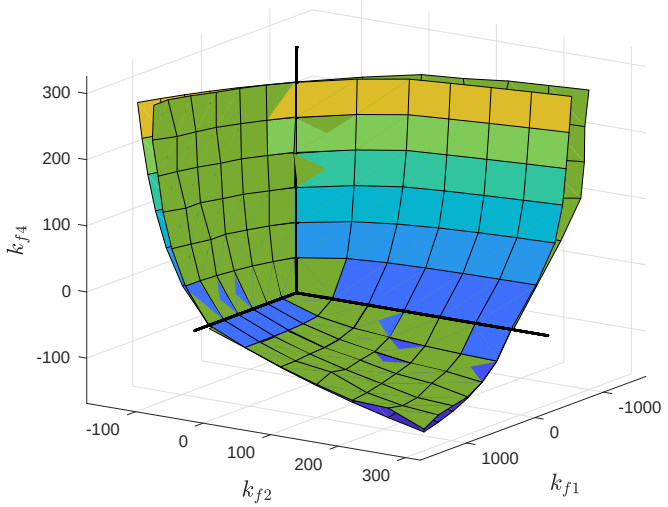

Fig. 9. Stability boundary obtained from small-signal stability analysis of the full-order model (green) compared against stability boundary constructed from the Nth-order model (colormap).

Figure 8 shows the performance lines intersecting the surface plot of the Nth-order model's stability boundary. Two kinds of disturbances are considered – Fig. 8(a) presents cases when AC disturbances occur in Area#1 and Fig. 8(b) presents cases when AC disturbances occur in Area#4. In each plot, several performance lines are considered, where each line corresponds to a particular prescribed ratio among the three participating areas' steady state frequency deviation. On each performance line of the form (23), the points for which $t \geq 0$ are marked by green and the points for which $t < 0$ are marked by red. Clearly, in both kind of disturbances, from Fig. 8(a) and (b), we see that the points on any performance line corresponding to $t > 0$ fall into the concave side of the stability boundary, which belongs to the stable region. On the other hand, points corresponding to $t < 0$ fall into the unstable region.

B. Stability Boundary Obtained from Full-order Model:

The Nth-order model is a representation that tries to capture the frequency dynamics of the realistic and detailed full-order model. The full-order nonlinear model consists of standard representation of the AC system, where all the generators are represented by sixth-order sub transient models equipped with type DC-1A excitation systems and detailed models of governors (with a ± 36 mHz dead band). The DC lines are modeled as one pi-section and the converters have standard vector control strategy with inner current-controllers. Thus far, the mathematical proof of the stability hypothesis, the unification theorem, and the validation through numerically constructed stability boundary – are all achieved based upon the Nth-order model. However, now small-signal stability analysis on the full-order model is used to numerically produce a closer-to-reality stability boundary, which is compared with that of the Nth-order model's stability boundary.

Figure 9 shows the stability boundary of the full-order model in green overlaid on the Nth-order model's stability boundary in colormap. Notice that both the boundaries have similar shapes and are closely matching with each other. Especially, near the regions of the three bold axes originating from

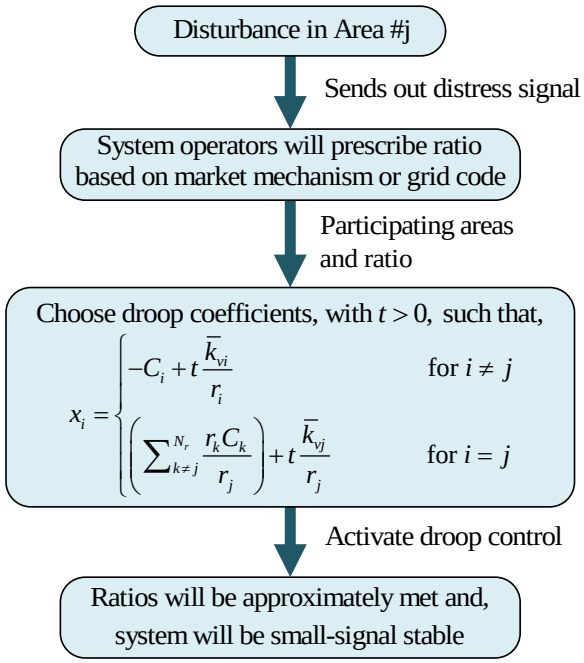

Fig. 10. Flow chart illustrating the proposed process following a disturbance in AC Area #j, in order to achieve the prescribed ratio and small-signal stability.

($-k_{gov1}$,$-k_{gov2}$,$-k_{gov4}$) the boundaries are most accurate. Since the performance lines are of the form (23) and since $\vec{a}_1$ has all positive components, we know that all points on the performance line with $t > 0$ lie inside the quadrant formed by the bold axes. On the other hand, the petals of both the stability boundaries are expanding away from the quadrant. Therefore, the stability hypothesis can be seamlessly extended to the full-order model.

VII. Nonlinear Time-Domain Simulation Studies

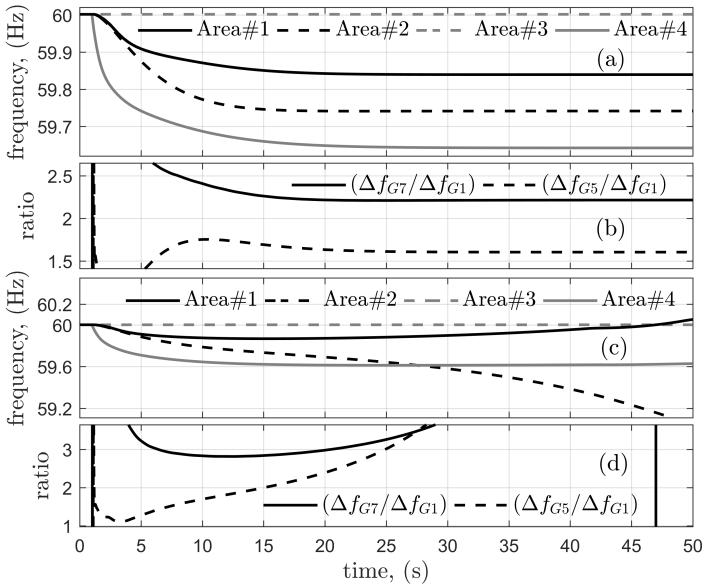

Fig. 11. Frequency dynamics following a 10% step reduction in generation of AC Area #4, when implemented in full-order nonlinear model with a prescribed ratio of 1 : 1.5 : NP : 2, where NP stands for non-participating.

Figure 10 illustrates how the ratios and droop coefficients are chosen following a disturbance. Due to simplicity of the equations, it is possible to compute the droop coefficients in real time with minimal information. In order to validate the stability hypothesis for Mode-III, time-domain simulation studies are performed on the full-order nonlinear model for two cases. An AC-side disturbance of 10% step reduction in generation of AC Area #4 is considered in both cases. Additionally, in both cases, inertial and frequency droop coefficients are designed to satisfy constraint (22). However, Case-I corresponds to frequency droop coefficients that are all greater than $-k_{govi}$, i.e, they belong to $\mathcal{L}_s$ of Theorem-II. Case-II on the other hand, does not satisfy the criterion from stability hypothesis. The parameters chosen for these cases are shown in the Appendix A. Figures 11 (a) and (b) validate the approximate ratio-tracking performance and stability in Case-I, while instability is observed in Figs 11 (c) and (d), which corresponds to Case-II.

VIII. Conclusion

The requirement on inertial and frequency droop coefficients to ensure small-signal stability in asynchronous AC-MTDC system was determined. To that end, using a reduced Nth-order model, a 'stability hypothesis' was formulated based on certain observations. The hypothesis was analytically proved for the cases when either one of the droops, primary frequency or inertial droop control is active. Moreover, implication of this hypothesis on a recently-proposed ratio-based frequency support method was analyzed by unifying stability and generalized performance criterion. The stability hypothesis was validated by studying numerically constructed stability boundaries in the frequency droop coefficient space. The stability boundary obtained from small-signal analysis of full-order nonlinear model was shown to approximately match the boundary obtained by the Nth-order model, which further strengthened the hypothesis. Finally, various time-domain simulation studies performed on full-order model supported the stability hypothesis.

Appendix A

System parameters: k_{gov1} = 212.20 MW/Hz, and k_{gov2} = k_{gov3} = k_{gov4} = 50.05 MW/Hz; H_{G1} = 228.15 s, H_{G2} = 185.25 s, and H_{G3} = H_{G4} = 74.1 s.

Inertial and frequency droop coefficients:

Area Number		#1	#2	#4
Case-I	h_i (s)	271.85	-18.58	378.01
	k_{fi} (MW/Hz)	287.79	113.62	270.89
Case-II	h_i (s)	271.85	-18.58	378.01
	k_{fi} (MW/Hz)	-362.21	-103.05	108.39

Note that H_{Gi}s and h_is are on a 100 MVA base.

Appendix B

Theorem-III: Given that disturbance occurred in Area#1 at $t = 0$, if matrices $\mathbf{K_{Nr}}$ and $\mathbf{H_{Nr}}$ satisfy the stability constraint (8) and the performance constraints (19) and (20), respectively, then the frequency deviation in participating areas Δf_i, i from 1 to N_r will be of the ratio $r_1 : \cdots : r_{Nr}$ $\forall$ $t > 0$ in the Nth-order model.

Proof: Consider the following differential equation,

$$2f_0(\sum_k^{N_r} r_k H_{Gk})\Delta\dot{f}^* = -(\sum_k^{N_r} r_k k_{govk})\Delta f^* - \Delta P_1 \tag{28}$$

The above system is clearly small-signal stable, due to positive summations on either side of equality. If constraints (19) and (20) are true then, by multiplying either side of (28) by $\hat{\mathbf{e}}_\mathbf{1}$, we get,

$$\begin{aligned} 2f_0\mathbf{H_{Nr}}\begin{bmatrix} r_1 & \cdots & r_{Nr}\end{bmatrix}^T\Delta\dot{f}^* = \\ -\mathbf{K_{Nr}}\begin{bmatrix} r_1 & \cdots & r_{Nr}\end{bmatrix}^T\Delta f^* - \Delta P_1\hat{\mathbf{e}}_\mathbf{1}\end{aligned} \tag{29}$$

We know that following the disturbance in Area#1, from (4), the dynamics in the AC-DC system are governed by,

$$\begin{aligned} 2f_0\mathbf{H_{Nr}}\begin{bmatrix} \Delta\dot{f}_1 & \cdots & \Delta\dot{f}_{Nr}\end{bmatrix}^T = \\ -\mathbf{K_{Nr}}\begin{bmatrix} \Delta f_1 & \cdots & \Delta f_{Nr}\end{bmatrix}^T - \Delta P_1\hat{\mathbf{e}}_\mathbf{1}\end{aligned} \tag{30}$$

Subtracting (29) from (30), and defining $\Delta f_i - r_i\Delta f^*$ as ΔF_i and $\mathbf{\Delta F}$ as a vector with ΔF_i as its ith entry, we get,

$$2f_0\mathbf{H_{Nr}}\mathbf{\Delta\dot{F}} = -\mathbf{K_{Nr}}\mathbf{\Delta F} \tag{31}$$

Initially, due to steady state, we have $\Delta F_i(0) = 0\ \forall\ i$. Since the disturbance term, ΔP_1 is eliminated in (31), following the disturbance, if the stability constraint (8) is satisfied, then $\Delta F_i(t)$ will remain at zero $\forall\ i, t > 0$. From the definition, this implies that $\Delta f_i(t) = r_i\Delta f^*(t)\ \forall\ i, t > 0$.

Remark-II: The state, Δf^* follows the frequency dynamics of a single machine whose inertia and inverse governor droop are $(\sum_k^{N_r} r_k H_{Gk})$ and $(\sum_k^{N_r} r_k k_{govk})$, respectively, and is always small-signal stable. If constraint (8) is not satisfied then $\Delta F_i(t)$ and $\Delta f_i(t)$ diverge from 0 and $r_i\Delta f^*(t)$, respectively.

REFERENCES

[1] J. Dai, Y. Phulpin, A. Sarlette, and D. Ernst, "Coordinated primary frequency control among non-synchronous systems connected by a multi-terminal high-voltage direct current grid," *IET Generation, Transmission Distribution*, vol. 6, no. 2, pp. 99–108, February 2012.

[2] A. Sarlette, J. Dai, Y. Phulpin, and D. Ernst, "Cooperative frequency control with a multi-terminal high-voltage DC network," *Automatica*, vol. 48, no. 12, pp. 3128 – 3134, 2012.

[3] F. D. Bianchi and J. L. Domnguez-Garca, "Coordinated frequency control using MT-HVDC grids with wind power plants," *IEEE Transactions on Sustainable Energy*, vol. 7, no. 1, pp. 213–220, Jan 2016.

[4] P. M. Namara, R. R. Negenborn, B. D. Schutter, G. Lightbody, and S. McLoone, "Distributed MPC for frequency regulation in multi-terminal HVDC grids," *Control Engineering Practice*, vol. 46, pp. 176 – 187, 2016.

[5] M. Andreasson, R. Wiget, D. V. Dimarogonas, K. H. Johansson, and G. Andersson, "Coordinated frequency control through MTDC transmission systems," *IFAC-PapersOnLine*, vol. 48, no. 22, pp. 106 – 111, 2015.

[6] ——, "Distributed frequency control through MTDC transmission systems," *IEEE Transactions on Power Systems*, vol. 32, no. 1, pp. 250–260, Jan 2017.

[7] P. McNamara and F. Milano, "Model predictive control-based AGC for multi-terminal HVDC-connected AC grids," *IEEE Transactions on Power Systems*, vol. 33, no. 1, pp. 1036–1048, Jan 2018.

[8] T. M. Haileselassie and K. Uhlen, "Primary frequency control of remote grids connected by multi-terminal HVDC," in *IEEE PES General Meeting*, July 2010, pp. 1–6.

[9] B. Silva, C. L. Moreira, L. Seca, Y. Phulpin, and J. A. P. Lopes, "Provision of inertial and primary frequency control services using offshore multiterminal HVDC networks," *IEEE Transactions on Sustainable Energy*, vol. 3, no. 4, pp. 800–808, Oct 2012.

[10] I. M. Sanz, B. Chaudhuri, and G. Strbac, "Inertial response from offshore wind farms connected through DC grids," *IEEE Transactions on Power Systems*, vol. 30, no. 3, pp. 1518–1527, May 2015.

[11] N. R. Chaudhuri, R. Majumder, and B. Chaudhuri, "System frequency support through multi-terminal dc (mtdc) grids," *IEEE Transactions on Power Systems*, vol. 28, no. 1, pp. 347–356, Feb 2013.

[12] N. R. Chaudhuri and B. Chaudhuri, "Adaptive droop control for effective power sharing in multi-terminal DC (MTDC) grids," *IEEE Transactions on Power Systems*, vol. 28, no. 1, pp. 21–29, Feb 2013.

[13] I. M. Sanz, B. Chaudhuri, and G. Strbac, "Frequency changes in AC systems connected to DC grids: Impact of AC vs. DC side events," in *2014 IEEE PES General Meeting — Conference Exposition*, July 2014, pp. 1–5.

[14] S. Akkari, J. Dai, M. Petit, and X. Guillaud, "Coupling between the frequency droop and the voltage droop of an AC/DC converter in an MTDC system," in *2015 IEEE Eindhoven PowerTech*, June 2015, pp. 1–6.

[15] L. Papangelis, X. Guillaud, and T. V. Cutsem, "Frequency support among asynchronous AC systems through VSCs emulating power plants," in *11th IET International Conference on AC and DC Power Transmission*, Feb 2015, pp. 1–9.

[16] L. Papangelis, M.-S. Debry, P. Panciatici, and T. V. Cutsem, "A receding horizon approach to incorporate frequency support into the AC/DC converters of a multi-terminal DC grid," *Electric Power Systems Research*, vol. 148, pp. 1 – 9, 2017.

[17] L. Papangelis, M. S. Debry, T. V. Cutsem, and P. Panciatici, "Local control of AC/DC converters for frequency support between asynchronous AC areas," in *2017 IEEE Manchester PowerTech*, June 2017, pp. 1–6.

[18] L. Papangelis, M.-S. Debry, T. Prevost, P. Panciatici, and T. V. Cutsem, "Decentralized model predictive control of voltage source converters for AC frequency containment," *International Journal of Electrical Power & Energy Systems*, vol. 98, pp. 342 – 349, 2018.

[19] R. Wang, L. Chen, T. Zheng, and S. Mei, "VSG-based adaptive droop control for frequency and active power regulation in the MTDC system," *CSEE Journal of Power and Energy Systems*, vol. 3, no. 3, pp. 260–268, Sept 2017.

[20] W. Wang, Y. Li, Y. Cao, U. Hger, and C. Rehtanz, "Adaptive droop control of VSC-MTDC system for frequency support and power sharing," *IEEE Transactions on Power Systems*, vol. 33, no. 2, pp. 1264–1274, March 2018.

[21] Y. Li and Z. Xu, "Coordinated control of wind farms and MTDC grids for system frequency support," *Electric Power Components and Systems*, vol. 45, no. 4, pp. 451–464, 2017.

[22] S. G. Vennelaganti and N. Ray Chaudhuri, "Controlled primary frequency support for asynchronous AC areas through an MTDC grid," in *2018 IEEE Power Energy Society General Meeting (PESGM)*, Aug 2018, pp. 1–5.

[23] S. G. Vennelaganti and N. R. Chaudhuri, "Selective power routing in MTDC grids for inertial and primary frequency support," *IEEE Transactions on Power Systems*, vol. 33, no. 6, pp. 7020–7030, Nov 2018.

[24] ——, "Ratio-based selective inertial and primary frequency support through MTDC grids with offshore wind farms," *IEEE Transactions on Power Systems*, vol. 33, no. 6, pp. 7277–7287, Nov 2018.

[25] B. Berggren, K. Lindn, and R. Majumder, "DC grid control through the pilot voltage droop concept–methodology for establishing droop constants," *IEEE Transactions on Power Systems*, vol. 30, no. 5, pp. 2312–2320, Sep. 2015.

[26] M. Zedek, "Continuity and location of zeros of linear combinations of polynomials," *Proc. Amer. Math. Soc.*, 16 (1965), 78-84.

Sai Gopal Vennelaganti (S'16) received his Bachelors degree in Electrical Engineering from Indian Institute of Technology Madras (IITM), Chennai, India in 2016. He joined the Ph.D. program of the Pennsylvania State University, University Park, PA in Fall 2016. His research interests include modeling and prevention of cascading failure in cyber-physical power systems, power electronic control applications in HVDC, Multi-terminal HVDC, Power Quality, Hybrid Microgrids and Smart grids.

Nilanjan Ray Chaudhuri (S'08-M'09-SM'16) received his Ph.D. degree from Imperial College London, London, UK in 2011 in Power Systems. From 2005-2007, he worked in General Electric (GE) John F. Welch Technology Center. He came back to GE and worked in GE Global Research Center, NY, USA as a Lead Engineer during 2011-2014. Presently, he is an Assistant Professor with the School of Electrical Engineering and Computer Science at Penn State, University Park, PA. He was an Assistant Professor with North Dakota State University, Fargo, ND, USA during 2014-2016. He is a member of the IEEE and IEEE PES. Dr. Ray Chaudhuri is the lead author of the book Multi-terminal Direct Current Grids: Modeling, Analysis, and Control (Wiley/IEEE Press, 2014). He served as an Associate Editor of the IEEE TRANSACTIONS ON POWER DELIVERY (2013 - 2019) and IEEE PES LETTERS (2016 - present). Dr. Ray Chaudhuri was the recipient of the National Science Foundation Early Faculty CAREER Award in 2016 and Joel and Ruth Spira Excellence in Teaching Award in 2019.